Charged particle multiplicities in heavy-ion-induced fission

H. Ikezoe, N. Shikazono, Y. Nagame, Y. Sugiyama, Y. Tomita, K. Ideno,
I. Nishinaka, B. J. Qi,* H. J. Kim,† and A. Iwamoto
Department of Physics, Japan Atomic Energy Research Institute, Tokai-mura, Ibaraki-ken 319-11 Japan

T. Ohtsuki
Laboratory of Nuclear Science, Tohoku University, Sendai-shi, Miyagi-ken 982, Japan
(Received 9 March 1992)

Pre- and post-scission protons and α particles are measured in the $^{16}O+^{197}Au$, $^{19}F+^{181}Ta$, ^{197}Au and ^{208}Pb, and $^{28}Si+^{197}Au$ and ^{208}Pb reactions in the compound nucleus excitation energy range of 43 to 117 MeV. The angular correlation measurements between α particles and fission fragments suggest that the pre-scission α particles seem to be mainly emitted from spherical compound nuclei or nuclei in an early stage of the fission process before saddle. The pre-scission multiplicities of protons and α particles are compared to the statistical model calculations and are reproduced by assuming the ratio a_f/a_n of the saddle point deformation to the ground-state deformation within the limit of 1.00 to 1.02. The post-scission protons and α particles are consistent with the evaporations from the fission fragments whose excitation energies are considerably reduced by the pre-scission neutron emissions.

PACS number(s): 25.85.Ge

I. INTRODUCTION

The time scale for excited heavy nuclei which result from a heavy-ion-induced fusion reaction to undergo fission has been studied extensively by measuring multiplicities of neutron [1–11], charged particles [12–15], and electric dipole γ rays [16–18]. From these, it has been inferred that the fission dynamics is a relatively slow process (10^{-20}–10^{-19} sec) even when the reaction leads to highly excited compound nuclei [10]. The fission time scale is generally believed to consist of two major parts: the transient time for the initial configuration to reach a stationary value at the saddle point and the descent time from saddle to scission. Thus it is very desirable to study both of these parts to better understand the fission dynamics. Although results from neutron and charged particle measurements are both useful to the time scale issue, owing to the added Coulomb repulsion, which can significantly affect the energy and direction of charged particles emitted in the early phase of fission, charged particle measurements can provide information pertaining to the first part of the fission time scale that is either difficult to obtain or unobservable from neutron results.

In this article we present the energy and angle distributions of protons and α particles observed in coincidence with fission fragments that result from fission of compound systems formed by ^{16}O, ^{19}F, and ^{28}Si bombardment of selected heavy targets at a number of energies with an emphasis on the time scale. Some parts of our findings on these systems have been published previously [19,20].

*On leave from Institute of Atomic Energy, Beijing 102413, China.

†On leave from Oak Ridge National Laboratory, Oak Ridge, TN 37831.

II. EXPERIMENTAL METHOD

Protons and α particles were measured in coincidence with fission fragments for the $^{16}O+^{197}Au$; $^{19}F+^{181}Ta$, ^{197}Au, and ^{208}Pb, and $^{28}Si+^{197}Au$ and ^{208}Pb systems at a number of incident energies. Some results from the $^{16}O+^{197}Au$ and $^{19}F+^{197}Au$ systems have already been reported [19,20]. Since the experimental arrangement and procedure for particle-fission correlation measurements are the same as those given in Refs. [19 and [20], only a brief description is given here.

Thin, self-supporting ^{181}Ta, ^{197}Au, and ^{208}Pb targets were bombarded with ^{16}O, ^{19}F, and ^{28}Si beams from the Japan Atomic Energy Research Institute (JAERI) tandem accelerator. Table I gives details of the targets and beams. Figure 1 give a schematic view of the detector placement for particle-fission correlation measurements. Four solid-state detector telescopes (ΔE and E) for light charged particles and two Si(Au) detectors for fission fragments were used. Solid angles subtended by fragment counters and telescope counters were about 50 and about 6 msr, respectively. Only large backward angles

TABLE I. Target thicknesses and bombarding energies used in the present experiments.

Reactions	Target thickness (mg/cm^2)	Bombarding energies (MeV)
$^{16}O+^{197}Au$	1.2	94.0–149.3
$^{19}F+^{181}Ta$	0.8,1.2	109.1–162.0
$^{19}F+^{197}Au$	1.2	92.0–162.0
$^{19}F+^{208}Pb$	0.78	114.6–162.4
$^{28}Si+^{197}Au$	1.1,1.2	147.2–194.1
$^{28}Si+^{208}Pb$	0.78,1.6[a]	156.7–188.8

[a]With carbon backing of 10 μg/cm^2.

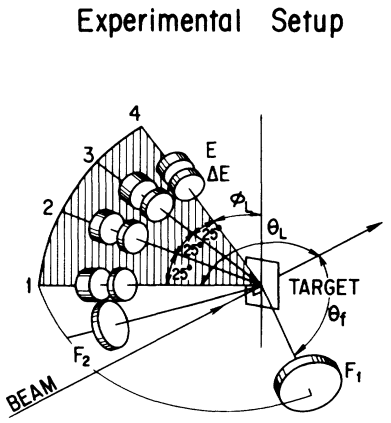

FIG. 1. Schematic diagram of the present experimental setup showing the fission detectors F_1 and F_2 and charged particle detector telescopes ΔE_i-E_i ($i=1,2,3,4$). The reaction plane is defined by the beam and F_1 detector. F_2 and telescope 1 are placed in the reaction plane, and the other telescopes are placed out of the reaction plane.

($\theta_f=123°-158°$) were covered by the Si(Au) detectors in order to emphasize fission fragment yield, not other reaction products. Pulse heights from these detectors showed no indication of significant contamination from deep-inelastic and other reactions at these backward angles for all cases. Telescope counters covered a number of angles, both in plane ($\theta_L=-125°$ and $-135°$) and out-of-reaction plane ($\phi_L=15°-90°$), which were chosen to provide differential as well as angle-integrated multiplicities.

The relative time intervals (50–80 nsec) of the signals from the telescope counters and fission counters were recorded to identify coincidence events. Protons and α particles that were in coincidence with fission fragments were selected from telescope events (particle identification was effected from the ΔE-E relation). Coincidence charged particle spectra obtained with the above-described arrangement after suitable intensity normalization to differential multiplicity are shown in Figs. 2 and 3 for illustrative cases. Normalization was effected by dividing coincidence intensities by corresponding singles fission fragment yields measured at the same angle as

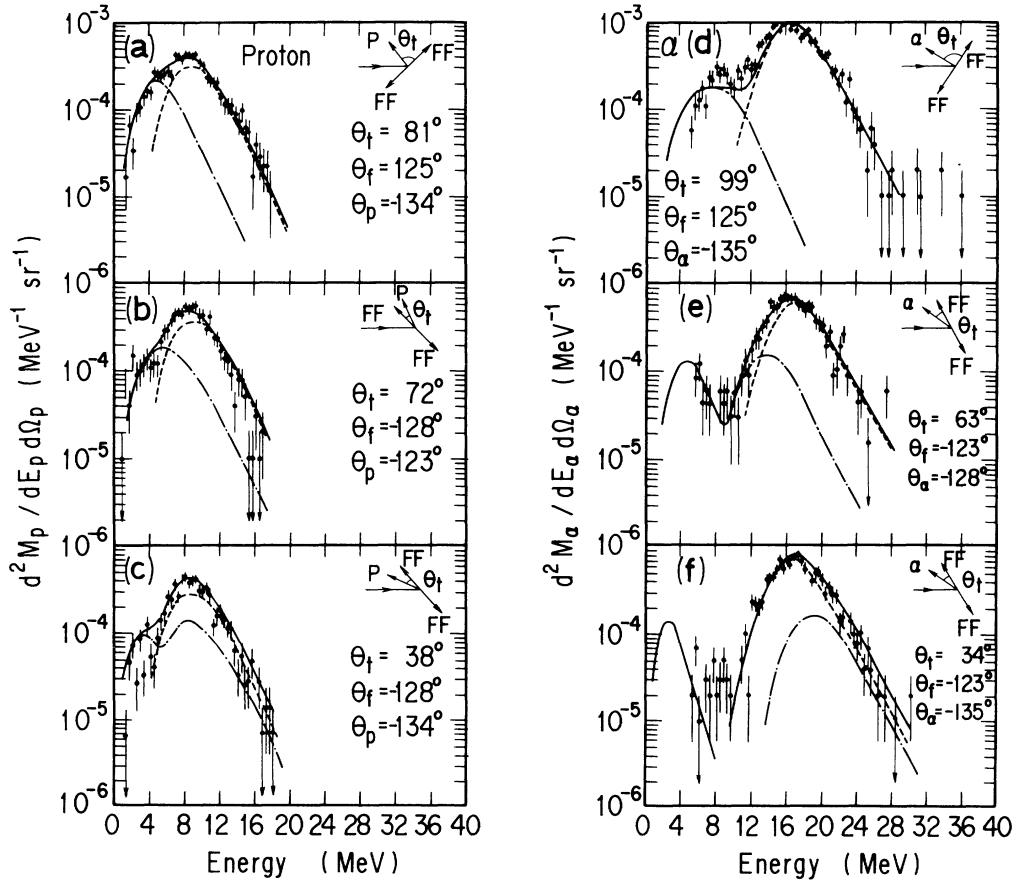

FIG. 2. (a)–(c) energy spectra of protons and (d)–(f) α particles in coincidence with fission fragments in the $^{19}F+^{181}Ta$ reaction with a bombarding energy of 146 MeV. The directions of the charged particles and fission fragments are shown schematically together with the angle θ_t between the charged particle and fission fragment in the c.m. system, the laboratory angle of the fission counter θ_f, and the telescope counter θ_p or θ_α. The negative angles mean the angles at the side opposite to the F_1 detector with respect to the beam. The calculated energy spectra of protons and α particles emitted from the compound nucleus (CE) and fission fragments (FE) are shown as the dashed and dot-dashed curves, respectively. The low-energy thresholds of the telescope counters were about 1 MeV for protons and 5 MeV for α particles. The high-energy cutoff of the proton spectra was due to the insufficient detector thicknesses to stop protons in the telescope counters.

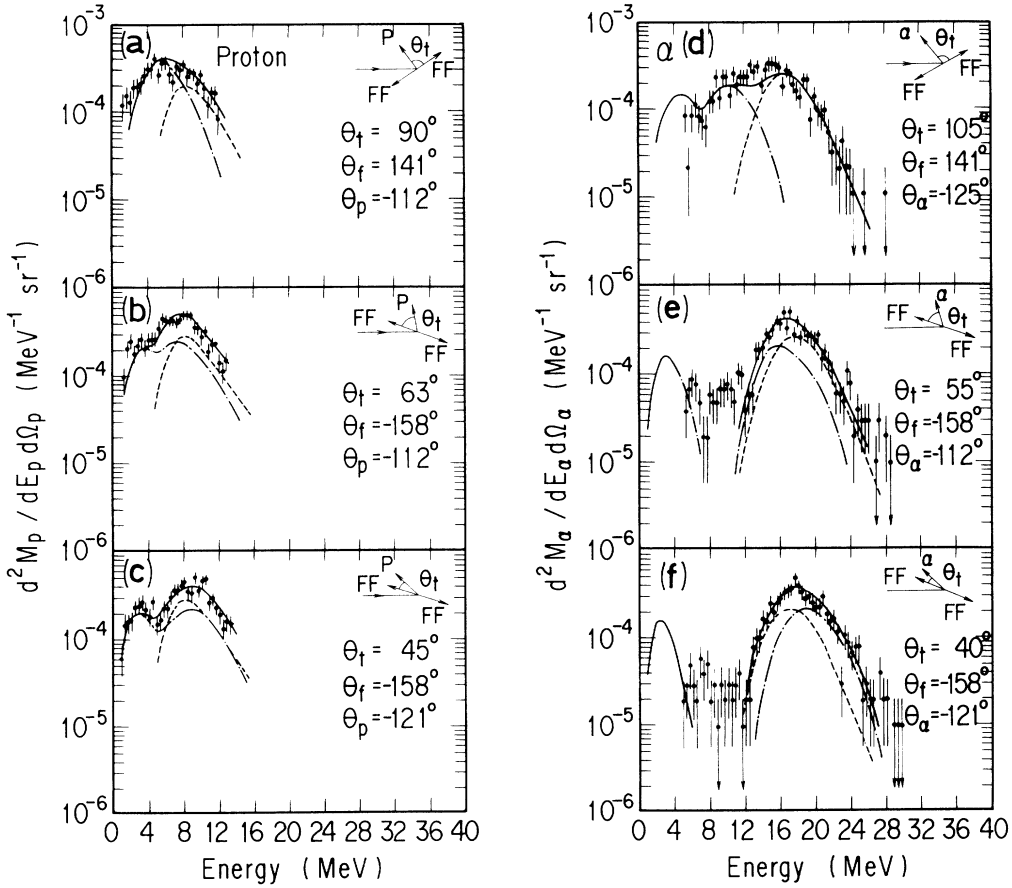

FIG. 3. Same as Fig. 2, but for the $^{28}Si + ^{197}Au$ reaction with a bombarding energy of 172.4 MeV.

in the correlation measurements. The relative angle θ_t between charged particle and fission fragments in the center-of-mass (c.m.) system are schematically shown in these figures, where the angles of telescopes, θ_L, are denoted as θ_p for protons and θ_α for αparticles. The curves accompanying the data are calculated spectra to be explained later.

Detailed singles angular distribution of fission fragments for the $^{19}F + ^{181}Ta$ reaction were measured for the same energy region covered in the correlation measurement. Values of the angular momentum fluctuation parameter K_0^2 and the average angular momentum $\bar{l}$ for fission that are needed for later discussion are obtained from analyzing results from this measurement. In order to identify and select fission fragments at more forward angles, the gas-ion chamber plus Si(Au) telescope that was used for the work reported in Ref. [19] was used. Measured angular distributions after conversion into the c.m. system by using the total kinetic energy of the fission fragments predicted by the systematics of Viola, Kwiatkowski, and Walker systematics [21] are shown in Fig. 4. Solid curves shown are fits to the data in terms of Legendre polynomials (even terms up to sixth order). Table II gives fission cross sections obtained from these differential cross sections. Our values agree well with those given by Refs. [22] and [23] earlier.

TABLE II. Fission cross sections, average angular momenta, and K_0 parameters measured in the $^{19}F + ^{181}Ta$ reaction.

E_{lab}	σ_{fiss} (mb)	$\bar{l}$ ($\hbar$)	K_0^2
99.2	152±23	34.7	97±10
109.2	428±43	41.3	110±10
114.2	578±58	43.8	118±12
119.2	721±70	45.6	128±15
124.2	835±84	47.7	147±15
129.3	937±90	49.2	157±15
135.3	1054±160	51.2	174±15
143.5	1262±130	54.6	195±20
151.3	1331±130	56.1	205±20
159.3	1434±140	58.1	220±20

III. EXPERIMENTAL RESULTS

A. Coincidence energy spectra

Energy-integrated differential multiplicities for protons and α particles were obtained from experimental coincidence spectra, such as those shown in Figs. 2 and 3, assuming emission from either the compound system (CE) prior to fission or from fully accelerated fission fragments

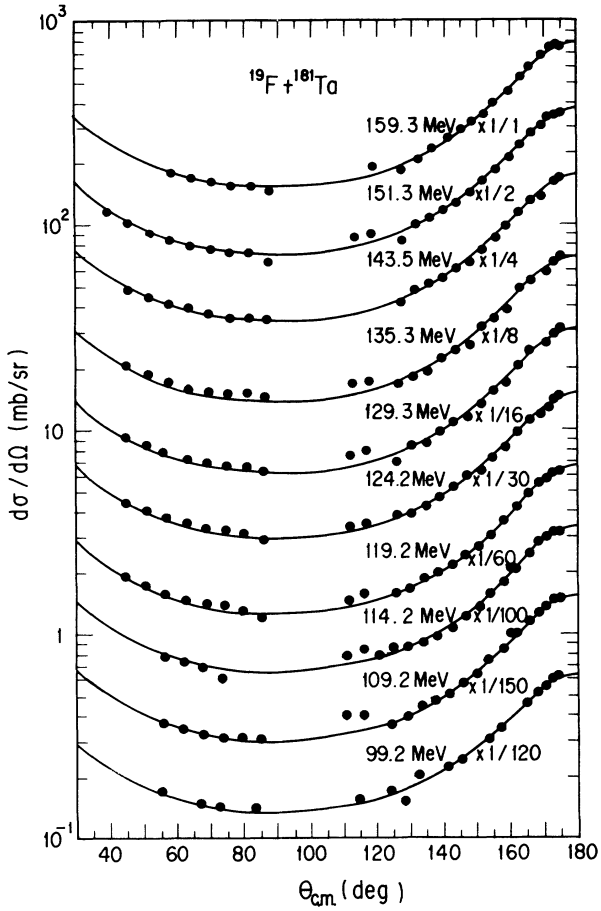

FIG. 4. Center-of-mass angular distributions of fission fragments measured in the $^{19}F+^{181}Ta$ reaction.

(FE) after fission. Small contributions from the near-scission configuration (NSE), which is sharply peaked in the direction perpendicular to the fission direction, are considered and are dealt with only as a contaminant in this paper. It will be the subject of a separate future paper.

Measured spectra were fitted to statistical-model calculations using the code PACE2 [24]. Details of the calculation are given in Sec. IV B. Here we just discuss how calculated emission spectra are utilized to obtain separate CE and FE contributions from measured coincidence spectra. Transmission coefficients needed to calculate CE and FE emission spectra were generated using the optical-model potentials of Perey [25] for protons and Huizenga and Igo [26] for α particles. However, as noted earlier in Refs. [19] and [20], emission barriers predicted by these optical-model potentials had to be lowered by certain amounts in order to fit the data well. The amount by which the barrier heights for CE emission were lowered in order to fit the data are given in Table III. The calculated CE spectra are shown in Fig. 2 and 3 as the dashed curves.

The FE energy spectra were calculated for particle evaporations from excited symmetric mass fragments by assuming the emission barrier lowered by an amount of

TABLE III. Emission barrier reductions for protons Δ_p and for α particles Δ_α.

Reactions	Barrier reductions (MeV) Δ_p	Δ_α
$^{16}O+^{197}Au$	1.0	1.8
$^{19}F+^{181}Ta$	1.2	1.8
$^{19}F+^{197}Au$	1.0	2.0
$^{19}F+^{208}Pb$	1.6	1.8
$^{28}Si+^{197}Au$	2.0	2.5
$^{28}Si+^{208}Pb$	2.0[a]	2.5[a]

[a]The statistics of the measured energy spectra was not enough to determine the emission barrier reductions. The measured values in the $^{28}Si + ^{197}Au$ reactions were used in the calculations of energy spectra and pre-scission charged particle multiplicities.

0.25 MeV for protons and 0.5 MeV for α particles compared with the emission barriers predicted by the optical-model potentials [25,26]. The reason for using these lowered emission barriers is explained in Sec. IV B. The calculated energy spectra were converted from the fragment-rest system to the laboratory system using the total kinetic energy of the fission fragments predicted by the systematics of Viola, Kwiatkowski, and Walker.

The shapes of the calculated FE spectra may be changed because of the mass and velocity distributions of fission fragments. This was checked by taking into account the measured fragment mass and velocity distributions in the $^{19}F+^{181}Ta$,^{197}Au and $^{28}Si+^{197}Au$ reactions. The fragment mass distribution was divided into five mass bins with an equal width, and five representative masses from each mass bin were selected. The FE spectra calculated for these fragments were summed with weights proportional to the measured mass distribution. The velocity distribution and opening angles of the fission counters (see Sec. III *B*) were taken into account in the system conversion from the fragment-rest system to the laboratory system. Finally, we obtained a spectrum which was only few percent wider in shape than the one calculated for symmetric mass fragments. Thus, for simplicity, the FE spectra calculated for symmetric mass fragments were used in the present analysis.

The calculated FE spectra are shown in Figs. 2 and 3 as the dot-dashed curves, which show two components (low- and high-energy components) corresponding to emissions from two fission fragments. The calculated peak energies of these two components strongly depend on the relative placement of the telescope counters (ΔE and E) and fission counters. These two components completely overlap each other to make one peak for the detector placement shown in Figs. 2(a), 2(b), 2(d), and 3(a).

The calculated CE and FE spectra were fitted to the measured coincidence spectra by adjusting the respective normalization constants N_{CE} and N_{FE}. The same normalization constant for each N_{CE} and N_{FF} was used for all coincidence spectra measured at various angles θ_L, θ_f, and θ_t within a fixed bombarding energy and reaction system. The N_{CE} and N_{FE} for CE and FE components

thus obtained were used to get energy-integrated differential multiplicities for both components. For the later discussion, we call CE the pre-scission component and FE the post-scission component.

Only in α-particle coincidence spectra were the NSE components observed at the angles near $\theta_t = 90°$ in the energy region between the FE and CE components as shown in Figs. 2(d) and 3(d). The angle- and energy-integrated NSE were only about 10% of angle- and energy-integrated CE multiplicities.

B. Pre- and post-scission multiplicities

The energy-integrated differential CE and FE multiplicities were converted by using Jacobians from the laboratory system to the c.m. system and the fragment-rest system, respectively. Here we consider the errors of the Jacobians originating from the system conversion processes due to broad energy distributions of protons, α particles, and fission fragments. In the case of the CE multiplicities, the conversion errors were less than 3% when the Jacobians were calculated by using the most probable velocity of the pre-scission protons and α particles. This is because the observed pre-scission proton and α-particle velocities were about an order of magnitude larger than the center-of-mass velocities of the present reaction systems. On the other hand, in the case of the FE multiplicities, the conversion was ambiguous, because the velocities of the fission fragments were broad in addition to broad energy distributions of the FE components and the large opening angles ($\pm 7.5°$) of the fission counters. The velocities of fission fragments have been measured by a time-of-flight method as reported in Ref. [27] in the $^{19}F + ^{181}Ta$, ^{197}Au and $^{28}Si + ^{197}Au$ reactions with the same bombarding energy range as listed in Table I. The measured widths [full width at half maximum (FWHM)] of the velocity spectra of fission fragments were 35–40 % of the most probable velocities in these reaction systems. Using this value, the conversion error was estimated for the FE component measured at angles near $\theta_t = 90°$, because the FE component separated enough from the CE component at these angles in the coincidence spectra [see Figs. 2(a) and 2(d) and also Figs. 3(a) and 3(d)] so that the FE component was identified definitely. By taking into account the broad velocity distributions of fission fragments, post-scission protons, and α particles and the opening angles of the fission counters, the conversion error was estimated to be $\pm 20\%$. This error was added to the experimental errors of the FE multiplicities.

Typical out-of-plane angular distributions of the c.m. differential multiplicity $dM/d\Omega_{\text{c.m.}}$ for pre-scission protons and α particles are shown in Fig. 5 for the $^{19}F + ^{181}Ta$ reaction. The out-of-plane angular distributions were fitted by the expression

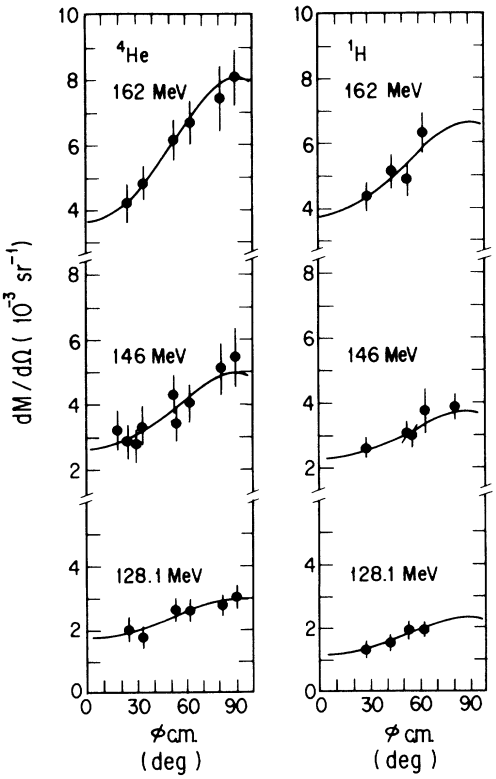

FIG. 5. Out-of-plane angular distributions of protons and α particles measured in coincidence with fission fragments in the $^{19}F + ^{181}Ta$ reaction. The angular distributions are fitted by Eq. (1) as shown by the solid lines.

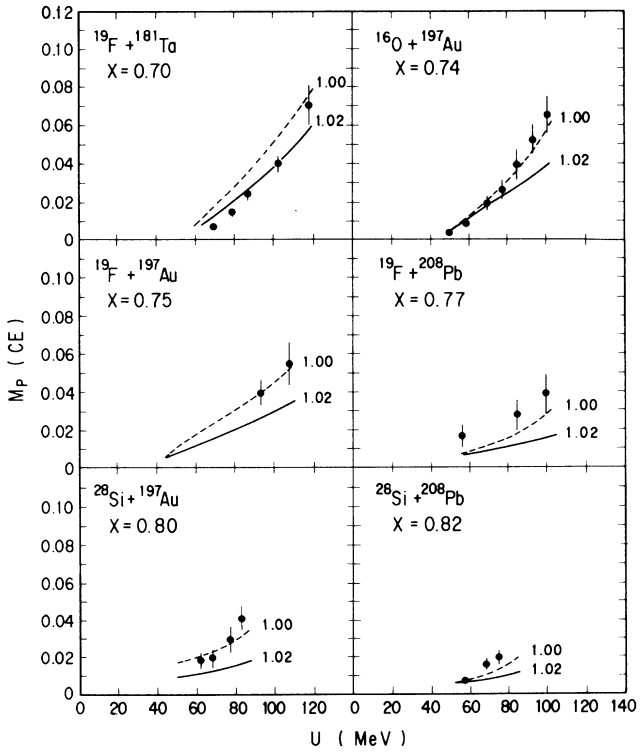

FIG. 6. Pre-scission proton multiplicities as a function of the compound nucleus excitation energy U. The reaction types and fissility X of the compound nuclei are shown. The dotted and solid curves represent the two statistical-model calculations, where the ratio a_f/a_n was assumed to be 1.00 and 1.02, respectively.

$$W_{\text{out}}(\phi_{\text{c.m.}}) = W_0 \exp[\beta_2 \sin^2(\phi_{\text{c.m.}})] \,, \quad (1)$$

where $\phi_{\text{c.m.}}$ is the center-of-mass angle of ϕ_L. The normalization constant W_0 and anisotropy parameter β_2 were obtained by the χ^2 fitting procedure and are listed in Table IV. The out-of-plane angular distributions for the pre-scission protons were isotropic in the present reactions except the $^{19}F+^{181}Ta$ and $^{16}O+^{197}Au$ reactions.

TABLE IV. Anisotropy parameters and pre- and post-scission multiplicities of protons and α particles.

E_{lab} (MeV)	U (MeV)	β_2^p	β_2^α	M_p^{pre}	M_α^{pre}	M_p^{post}	M_α^{post}
				$^{16}O+^{197}Au$			
94.0	48.3	0.0	0.0	0.003(1)	0.012(3)	0.004(2)	0.009(3)
104.1	57.6	0.0	0.0	0.007(2)	0.018(4)	0.005(2)	0.010(3)
116.1	68.7	0.0	0.0	0.018(4)	0.033(7)	0.009(3)	0.011(3)
124.1	76.2	0.12	0.15	0.025(5)	0.041(6)	0.011(3)	0.014(4)
132.5	83.9	0.0	0.18	0.038(8)	0.049(7)	0.014(4)	0.017(4)
141.2	91.9	0.12	0.16	0.051(8)	0.063(9)	0.017(5)	0.026(7)
149.3	99.4	0.12	0.24	0.064(10)	0.083(12)	0.018(5)	0.019(5)
				$^{19}F+^{181}Ta$			
109.1	68.9	0.0	0.28	0.006(1)	0.008(1)	0.008(2)	0.010(2)
113.9	73.2		0.16		0.014(2)		0.011(3)
119.2	78.0	0.0	0.69	0.014(2)	0.017(3)	0.010(3)	0.009(2)
128.1	86.1	0.71	0.54	0.023(4)	0.031(5)	0.014(4)	0.012(3)
146.0	102.3	0.50	0.61	0.040(4)	0.050(7)	0.018(5)	0.016(4)
162.0	116.8	0.56	0.79	0.070(10)	0.079(11)	0.024(6)	0.027(7)
				$^{19}F+^{197}Au$			
92.0	43.4		0.0		0.014(3)		0.008(3)
99.0	49.8		0.0		0.019(4)		0.009(3)
101.8	52.3		0.0		0.017(3)		0.008(3)
106.1	56.2		0.0		0.025(5)		0.010(3)
108.9	58.8		0.0		0.021(4)		0.011(3)
114.2	63.6		0.10		0.026(5)		0.012(3)
118.9	67.9		0.17		0.026(5)		0.013(3)
124.9	73.4		0.25		0.035(6)		0.015(4)
131.0	78.9		0.21		0.047(7)		0.019(5)
137.0	84.4		0.24		0.054(10)		0.018(5)
143.0	89.9		0.13		0.066(10)		0.020(5)
146.0	92.7	0.0	0.25	0.039(7)	0.060(10)	0.024(7)	0.018(5)
162.0	107.2	0.0	0.49	0.054(11)	0.075(11)	0.032(9)	0.030(7)
				$^{19}F+^{208}Pb$			
114.6	55.2	0.0	0.0	0.015(5)	0.028(9)	0.012(6)	0.013(3)
146.4	84.3	0.0	0.69	0.026(6)	0.038(7)	0.023(7)	0.019(5)
162.4	99.0	0.0	0.31	0.037(8)	0.052(8)	0.023(7)	0.019(5)
				$^{28}Si+^{197}Au$			
147.2	45.5		0.07		0.012(3)		a
152.78	50.4					0.014(4)	0.015(4)
160.4	57.1		0.40		0.024(5)		a
165.5	61.6	0.0	0.36	0.018(4)	0.023(3)	0.025(6)	0.029(7)
172.4	67.6	0.0	0.47	0.019(5)	0.025(4)	0.029(8)	0.029(7)
173.9	68.9					0.027(7)	0.033(8)
177.7	72.2		0.43		0.047(7)		0.045(10)
182.5	76.4	0.0	0.12	0.029(7)	0.035(5)	0.040(10)	0.050(12)
189.5	82.6	0.0	0.25	0.040(7)	0.051(7)	0.055(13)	0.059(15)
189.9	82.9					0.045(11)	0.046(11)
194.1	86.6		0.47		0.065(10)		0.061(15)
				$^{28}Si+^{108}Pb$			
156.7	45.5		0.17		0.010(2)	0.013(4)	0.015(4)
166.4	54.1		0.47		0.009(3)	0.022(7)	0.020(6)
168.8	56.2	0.0	0.0	0.005(2)	0.015(4)	0.014(4)	0.020(6)
174.4	61.2		1.3		0.016(5)	0.019(6)	0.026(8)
181.8	67.7	0.0	0.0	0.014(3)	0.029(7)	0.019(6)	0.027(8)
188.8	73.8	0.0	0.08	0.017(4)	0.032(8)	0.023(6)	0.034(10)

[a]The threshold energies of the telescope counters were too high to detect the post-scission charged particles.

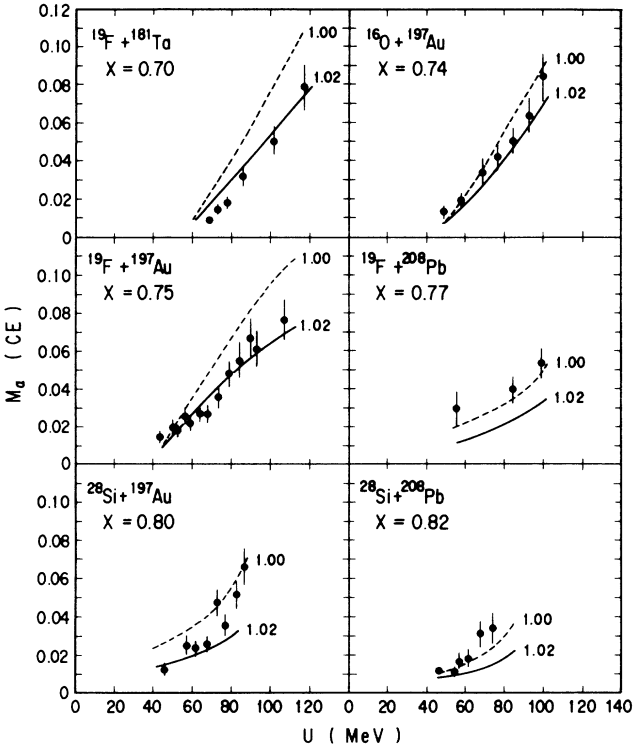

FIG. 7. Same as Fig. 6, but for the pre-scission α-particle multiplicities.

The pre-scission multiplicities M^{pre} of protons and α particles were obtained by integrating the out-of-plane angular distribution.

The post-scission differential multiplicities of protons and α particles were isotropic in the fragment-rest system. The angle-integrated multiplicities M^{post} were the sum of two contributions from both fission fragments.

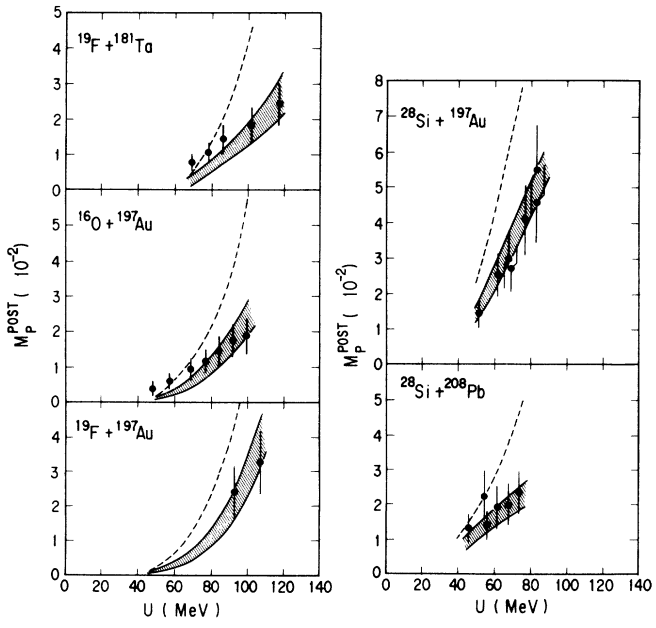

FIG. 8. Same as Fig. 6, but for the post-scission proton multiplicities. The two statistical-model calculations are shown as the shaded area and dashed curves, where the pre-scission neutron multiplicity ν_n was taken from the observed data ($\nu_n = \nu_n^{\text{obs}}$) and calculated ($\nu_n = \nu_n^{\text{cal}}$) by PACE2, respectively.

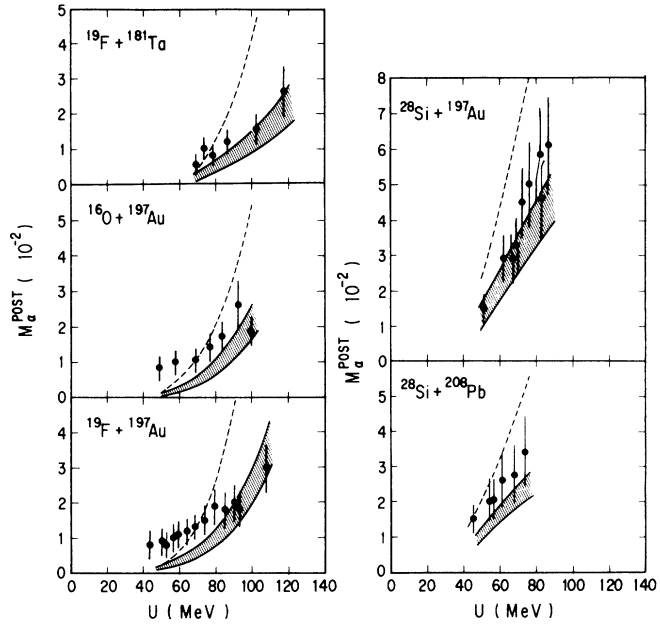

FIG. 9. Same as Fig. 8, but for the post-scission α-particle multiplicities.

The obtained pre- and post-scission multiplicities (M^{pre} and M^{post}) are listed in Table IV and plotted in Figs. 6–9 as a function of the excitation energy U of the compound nucleus,

$$U = E_{\text{c.m.}} + M_p + M_t - M_{\text{cn}} ,$$

where $E_{\text{c.m.}}$ is the center-of-mass bombarding energy and M_p, M_t, and M_{cn} are the mass excesses of the projectile, target, and compound nucleus, respectively. The mass excess M_{cn} was taken from the liquid-drop mass and M_p and M_t from the experimental ground-state masses.

IV. DISCUSSION

A. Out-of-plane angular distribution

Before discussing the pre- and post-scission multiplicities, we would like to discuss where pre-scission charged particles are emitted in the fission process (the pre- or post-saddle regions). Since out-of-plane angular distributions and energy spectra of charged particles are affected by the amount of emitter deformations when they are emitted, we investigated these effects in detail by analyzing the measured out-of-phase angular distributions and energy spectra of the pre-scission α particles in the ^{19}F + ^{181}Ta reaction.

It is important to take into account the angular momentum fluctuation of the compound nucleus in the particle-fission correlation measurement, because a wide K distribution considerably smears out the out-of-plane angular distribution, where K is the angular momentum

projection on the symmetric axis of the saddle point deformation [28]. The K distributions in the $^{19}F+^{181}Ta$ reactions were obtained by fitting the measured fission fragment angular distributions shown in Fig. 4 with the expression [28]

$$W(\theta) \propto \sum_{l=l_{ER}}^{\infty} (2l+1)T_l \times \sum_{K=-l}^{l} \frac{(2l+1)|d^l_{0,K}(\theta)|^2 \exp(-K^2/2K_0^2)}{\sum_{K=-l}^{l} \exp(-K^2/2K_0^2)}, \quad (2)$$

where $d^l_{0,K}(\theta)$ is the symmetric top wave function. The K distribution is assumed to be a Gaussian distribution with parameter K_0. We used the transmission coefficient T_l for fission, which was obtained by Hinde *et al.* [22] in the $^{19}F+^{181}Ta$ reaction. The obtained K_0^2 values are listed in Table II. The average angular momentum $\bar{l}$ for fission listed in Table II was obtained from the measured fission cross sections and T_l.

The out-of-plane angular distribution of emitted α particles due to a finite K_0 value has been studied by Schmitt and Srivastava [29] in the particle-fission correlation measurements. By using the expressions (3) and (4) of Ref. [29], the observed K_0 values, and the average angular momenta $\bar{l}$, the anisotropy parameter β_2^*, which is expected in the ideal spin orientation ($K_0=0$), was obtained from the observed out-of-plane angular distributions. The obtained anisotropies $A \equiv W_{out}(90°)/W_{out}(0°) = \exp(\beta_2^*)$ are listed as A_{expt} in Table V.

For comparison, the anisotropy $A_{sph}=\exp(\beta_2^{sph})$ for a spherical emitter was calculated by using the expression [30,31]

$$\beta_2^{sph} = \frac{(\bar{l}+0.5)^2}{2T\mathcal{J}} \frac{\mu R^2}{\mathcal{J}+\mu R^2},$$

where T and $\mathcal{J}$ are the nuclear temperature and moment of inertia of the spherical daughter nucleus, μ the reduced mass of the daughter nucleus and α particle, and R the barrier radius [32]. The moment of inertia was calculated with the radius parameter $r_0=1.225$ fm. The nuclear temperature T was calculated as

$$a_n T^2 = U - E_r - E_s - E_\alpha,$$

where the level-density parameter $a_n=19.6$ MeV^{-1} was used for the daughter nucleus ^{196}Hg, and with E_r the rotation energy, E_s the α-particle separation energy, and E_α the kinetic energy of the α particle. The separation energy E_s was -3.3 MeV, and E_α was calculated by PACE2. The rotation energy E_r at the average angular momentum $\bar{l}$ was calculated by the rotating finite-range model [33]. The calculated anisotropies A_{sph} are shown in Table V and are close to the observed value A_{expt}.

For the α-particle emissions from deformed nuclei, the anisotropy A becomes larger than A_{sph}, because the emission barrier height for α particles becomes small at the tip of the long axis ($\phi_t=0°$), and the spinoff energy [34] ($\sim$0.2 MeV) is very small for the present heavy compound nuclei; thus, low-energy α particles can be emitted to the direction ($\phi_t=0°$). This is simulated by statistical-model calculations for a deformed emitter [34]. For example, in the case of the saddle point deformation of ^{196}Hg, the emission barrier height for α particles at the tips of the long axis is expected to be 7–8 MeV smaller and slightly higher (<1 MeV) at the short axis than the barrier height predicted for the spherical nucleus [35]. If the pre-scission α particles are emitted from a highly deformed shape such as the saddle shape or the shapes in the saddle-to-scission region, we expect a large energy difference in respective α-particle spectra emitted at the long and short axes. The energy spectra measured in the geometry closest to $\phi_t=0°$ are shown in Fig. 2(f), where one of the telescope counters and the fission counter F_2 (see Fig. 1) were placed so that the low-energy tail of the CE component did not overlap with the FE components. If the low-energy α particles as mentioned exist, they could be observed in the energy region from 8 to 16 MeV in Fig. 2(f). Although the small yields are observed in the energies from 6 to 12 MeV in these figures, the low-energy regions (8–16 MeV) of the measured spectra are excellently reproduced all over by the calculated CE components.

As shown in Figs. 2 and 3, the measured coincidence energy spectra of the pre-scission protons and α particles were well reproduced by statistical-model calculations with the slightly lowered emission barriers as listed in Table III. The causes of the barrier lowering have been extensively studied in relation to emitter deformation [41]. The problem is still unresolved. Emitter deformation alone cannot give a consistent explanation for protons and α particles [42]. Here we emphasize that the out-of-plane anisotropy of the pre-scission α particles is a quantity sensitive to the moments of inertia and thus to deformation of the emitter, and based on the observed anisotropies, the pre-scission α particles are seen to be mainly emitted from the spherical or near-spherical compound nucleus. This is consistent with the statistical-model prediction for α-particle emissions, which shows that α particles tend to be emitted from the early decay steps of the compound nucleus.

TABLE V. Anistropies measured in the $^{19}F+^{181}Ta$ reaction.

E_{lab} (MeV)	U (MeV)	T (MeV)	$\bar{l}$ ($\hbar$)	K_0^2	A_{expt}	A_{sph}
128.1	86.1	1.61	48.7	155±15	2.2±0.2	2.3
146.0	102.3	1.79	54.6	196±20	2.5±0.2	2.6
162.0	116.8	1.95	58.6	225±20	3.5±0.5	2.8

For the pre-scission protons, we could not specify where they emit. This was because the CE and FE spectra of protons were so close in energy that it was impossible to observe the low-energy protons emitted at the long axis of deformed nucleus.

B. Statistical-model calculations

The measured pre- and post-scission multiplicities of protons and α particles were compared with statistical-model calculations using the code PACE2. The level-density parameter a_n for the ground-state deformation was assumed to be $A/10$, where A is the mass number of the nucleus. The same values for the fission barrier height B_f and the diffuseness parameter δ for the transmission coefficient T_l as those used in Ref. [5] were used for the $^{19}F+^{181}Ta$ and $^{16}+O+^{197}Au$ reactions. For the other reactions, B_f was calculated with the rotating finite-range model and $\delta=6\hbar$ was assumed. The calculated values of the multiplicities are sensitive to the emission barrier heights for charged particles and also the level-density parameter ratio a_f/a_n of the saddle point deformation to the ground-state deformation. The neutron multiplicity data [36] measured at low excitation energies limit the value of a_f/a_n within 1.02 ± 0.02. Therefore the ratio was changed within this limit in the present calculations. The lowered barrier for proton and α-particle emissions as mentioned in Sec. IV A were taken into account.

As for the proton and α-particle emissions from fission fragments, it was difficult to obtain the precise emission barrier heights for these particles in the present measurements because of the insufficient statistics for the FE components and also the partial overlap of the CE and FE components in energy. These emission barriers were estimated from the proton and α-particle evaporation spectra observed in the decay of the compound nucleus ^{98}Mo produced in the $^{86}Kr+^{12}C$ reaction [37], because the masses of symmetric fission fragments produced in the present reactions are close to the mass of ^{98}Mo. We fitted the reported evaporation spectra of protons and α particles with spectra calculated by adjusting the emission barriers for these particles by using PACE2. The best fit was obtained by assuming small barrier lowering ($\Delta_p=0.25$ MeV for protons and $\Delta_\alpha=0.5$ MeV for α particles) compared with the emission barriers predicted by the standard optical-model potential parameters of Perey for protons and Huizenga and Igo for α particles. These barrier lowerings are smaller than those of Ref. [37], but rather consistent with the results of Fornal *et al.* [38]. These lowered barriers were used to calculate the post-scission multiplicities. This modification of the barrier heights causes the 20–30% increases of the calculated values of M_p^{post} and M_α^{post} compared with the calculations with no barrier lowering, $\Delta_p=\Delta_\alpha=0$.

C. Pre-scission multiplicity

The calculated pre-scission multiplicities M_p^{pre} and M_α^{pre} are shown as the dashed curves ($a_f/a_n=1.00$) and solid curves ($a_f/a_n=1.02$) in Figs. 6 and 7. As shown in these figures, the calculated results are very sensitive to the values of a_f/a_n especially at high excitation energies. The calculated results increase more rapidly with decreasing a_f/a_n values. Almost all the data points are in between these two curves, and the observed trends as a function of U are nearly reproduced by the present calculations. In the ^{28}Si-induced reactions, however, the observed data tend to increase more rapidly than the calculated results. The calculated results slightly overestimate both charged particle multiplicities at low excitation energies in the $^{19}F+^{181}Ta$ reaction. In this reaction the pre-scission neutron multiplicities have been measured by Hinde *et al.* [5] and Newton *et al.* [8] and the statistical model calculations assuming the values of $a_f/a_n=0.98-1.02$ are in good agreement with the pre-scission neutron data at low excitation energies $U\leq70$ MeV [8]. Although in the $^{19}F+^{181}Ta$ reaction the calculations with $a_f/a_n=1.04$ agree better with both the pre-scission proton and α-particle multiplicity data at low excitation energies, these calculations fail to reproduce the pre-scission neutron multiplicity at the same low excitation energies.

On the other hand, it is well known that, although the pre-scission neutron data [5,6,8] agree with statistical-model calculations (assuming $a_f/a_n=1.00$) at low excitation energies $U\leq60$ MeV, these are considerably larger (2 times or more) at $U\geq60$ MeV than the statistical-model predictions. (The present statistical-model calculations give the same results as those of Refs. [5,6,8].)

The calculated charged particle multiplicities are also very sensitive to the values of their emission barrier heights. As shown in Ref. [9], the calculated results obtained by assuming the normal barrier heights that are predicted by the optical-model potentials mentioned in Sec. III A considerably underestimate the pre-scission α-particle multiplicity even at low excitation energies $U\leq60$ MeV, where the effect of fission dynamics on the pre-scission particle multiplicity is negligible [5,8]. We emphasize that only if the observed lowered barriers are used in the calculations with the limited values of $a_f/a_n=1.00-1.04$ are the low-energy multiplicity data of protons and α particles reasonably well reproduced.

The excess pre-scission neutrons over the statistical-model calculations have been considered to be due to a long transient time or a long saddle-to-scission time or the sum of both time intervals. If the whole excess pre-scission neutrons are, for instance, caused by the long transient time of 7×10^{-20} sec [5], the calculated M_p^{pre} and M_α^{pre} become larger by an amount of more than 2 times at the excitation energy range $U\geq60$ MeV [19]. This is contrary to the present results of the charged particle data.

As mentioned in Sec. IV A, the pre-scission α particles are seen to be mainly emitted from spherical nuclei or nuclei in early stage of the fission process before saddle, and then the pre-scission α particle multiplicities may be insensitive to the saddle-to-scission time, suggesting that the multiplicities are only affected by the transient time. Here we estimated the upper limit of the transient time from the pre-scission charged particle data by taking into

account the experimental errors of these data and the uncertainty (± 0.02) of a_f/a_n in the calculations. The statistical-model calculations taking into account the transient time have been reported in Ref. [19]. The estimated upper limit is 1.0×10^{-20} sec for the ^{16}O- and ^{19}F-induced reactions and 3×10^{-20} sec for the ^{28}Si-induced reactions. The absolute value of these values are ambiguous (factor of 2 or so) because of ambiguities in fission barrier heights, particle emission barrier heights, and level-density parameters (a_n and a_f) in the statistical-model calculations. However, we emphasize that the pre-scission neutron multiplicity data increase more rapidly with U than statistical-model predictions, while the pre-scission charged particle multiplicity data follow the predicted trends as a function of U. Therefore the pre-scission neutron data need longer fission time scales (10^{-20}–10^{-19} sec [1–18]) than the present upper limits in order to reproduce the neutron data by the same statistical-model calculations as shown here. The present analysis suggests that the major part of the excess pre-scission neutrons over the statistical-model predictions may be emitted from the saddle-to-scission region. A similar conclusion has been reported by Lestone *et al.* [15], where the pre-scission α-particle multiplicity data limit the transient time to $\sim1\times10^{-20}$ sec, and a long saddle-to-scission time of $\sim5\times10^{-20}$ sec is needed to account for the pre-scission neutron multiplicity data.

D. Post-scission multiplicity

The post-scission charged particle multiplicities contain an important information about the residual excitation energy of fission fragments. The post-scission neutron data indicate that the fragment excitation energies are about 50–60 MeV [7,11] irrespective of the compound nucleus excitation energy U. This was checked by comparing the observed $M_p^{\rm post}$ and $M_\alpha^{\rm post}$ to statistical-model calculations. At first, the fragment excitation energies were estimated by subtracting the energies removed by the pre-scission neutron emissions from the initial excitation U. After that, the statistical-model calculations for excited fission fragments were carried out to see how well the calculations reproduce the measured post-scission charged particle multiplicities.

The sum of the excitation energy, E_1+E_2, of both fission fragments is written as

$$E_1+E_2=E_{\rm c.m.}+Q_{\rm eff}-\nu_n k_n \ ,$$

$$Q_{\rm eff}=M_p+M_t-M_1-M_2-\nu_n M_n-{\rm TKE} \ ,$$

where M_1, M_2, and M_n are the mass excesses of the two fission fragments and neutron. The liquid-drop mass excesses were used for M_1 and M_2. The total kinetic energy (TKE) of the fission fragments produced after emissions of some pre-scission neutrons was estimated by the systematics of Viola, Kwiatkowski, and Walker [21]. ν_n is the pre-scission neutron multiplicity. The average neutron kinetic energy k_n was calculated by PACE2. The particle evaporations from the symmetric mass fragments were calculated by assuming $E_1=E_2$. The neutron to proton ratio N/Z of the fission fragment was assumed to be the same as the compound nucleus before fission. The angular momentum of each fission fragment was estimated to be $10\hbar$ from the γ-ray multiplicity data [39]. The angular momentum distribution was also taken into account in the calculations by assuming the Gaussian distribution with a FWHM$=4.3\hbar$ [40]. The calculated results were not sensitive to the distribution. The pre-scission neutron multiplicities ν_n were taken from Ref. [6], where the observed ν_n are compiled every compound nucleus fissility. The linear dependence of ν_n on U was assumed to estimate ν_n at a certain value of U. The experimental errors (±0.3 to ±0.5 amu [5,6]) of ν_n were also taken into account in the calculations. The calculated results are shown in Figs. 8 and 9 as the shaded areas.

The excitation energy of the fission fragment increases slowly, for instance, from 23 to 30 MeV as U increases from 70 to 117 MeV in the ^{19}F+^{181}Ta reactions, while the calculated post-scission multiplicity increases very rapidly by 6–8 times in the same excitation energy region. This rapid increase is due to the fact that the Q values for the proton and α-particle emissions from the fission fragments increase as the mass number of the fission fragments decrease with increasing pre-scission neutrons without changing the atomic number. It turns out that the emission probabilities of protons and α particles increase with ν_n.

As shown in Figs. 8 and 9, the overall trends of $M_p^{\rm post}$ and $M_\alpha^{\rm post}$ as a function of U are reproduced by the present calculations. There are some discrepancies between the data and the calculations in the low-energy regions of the ^{16}O+^{197}Au and ^{19}F+^{197}Au reactions. These discrepancies could not be dissolved by changing the parameters used in the present calculations within a reasonable range. The calculations for asymmetric mass fragments were also carried out, but the calculated results for $M_p^{\rm post}$ and $M_\alpha^{\rm post}$ became even smaller.

For comparison, the calculations for $M_p^{\rm post}$ and $M_\alpha^{\rm post}$ by using $\nu_n^{\rm cal's}$, which was estimated by PACE2 without taking into account the fission time scale, were carried out. The calculated results are plotted as the dashed lines in Figs. 8 and 9. It should be remembered that the $\nu_n^{\rm cal's}$ considerably underestimate the pre-scission neutron multiplicity data at $U\geq60$ MeV. In fact, the calculated results (dashed lines) considerably overestimate the post-scission multiplicities for all reaction systems studied here. This result suggests that the excitation energies, more than predicted by the statistical-model calculation, are in fact removed from the compound nucleus by the pre-scission neutron emissions, and then few excitation energies are left at scission. Hence the observed post-scission charged particle multiplicity data are consistent with the observed pre-scission neutron multiplicity data.

V. SUMMARY AND CONCLUSIONS

The pre- and post-scission protons and α particles have been measured in the ^{16}O+^{197}Au; ^{19}F+^{181}Ta, ^{197}Au, and ^{208}Pb; and ^{28}Si+^{197}Au and ^{208}Pb reactions. The emission mechanism of the pre-scission α particles were studied in detail in the ^{19}F+^{181}Ta reaction. The observed out-of-

plane angular distributions for the pre-scission α particles were close to those expected in emissions from the spherical compound nucleus. The measured coincidence energy spectra of the pre-scission protons and α particles were well reproduced by statistical-model calculations with slightly lowered emission barriers. We did not observe the extremely low-energy α particles (except the NSE), which may be emitted from deformed nuclei such as the saddle shape or more deformed nuclei in the saddle-to-scission region. The observed out-of-plane anisotropies suggest that the pre-scission α particles are seen to be mainly emitted from spherical nuclei or nuclei in an early stage of the fission process before saddle.

The observed pre-scission multiplicities for protons and α particles were compared with the statistical-model calculations. Both multiplicities nearly agree with the calculations with $a_f/a_n = 1.00$ and 1.02 without taking into account the transient time in the calculations. It seems that the transient time is rather short. On the other hand, the pre-scission neutron data reported up to now suggest a long transient time or a long saddle-to-scission time. The reason for this contradiction is not clear. However, if the charged particles (especially α particles) are more likely emitted in the pre-saddle region than the post-saddle region, as inferred from the observed out-of-plane anisotropy, the major part of the reported excess pre-scission neutrons over statistical-model calculations may be emitted in the saddle-to-scission region.

The observed post-scission multiplicities for protons and α particles are analyzed by statistical-model calculations, where the excitation energies of the fission fragments were estimated by using the observed pre-scission neutron multiplicity data. The observed trends as a function of U were roughly reproduced by the calculations, suggesting that the post-scission charged particles are emitted from the fission fragments whose excitation energies are considerably reduced by the pre-scission neutron emissions.

[1] E. Holub, D. Hilscher, G. Ingold, U. Jahnke, H. Ort, and H. Rossner, Phys. Rev. C **28**, 252 (1983).

[2] A. Gavron, A. Gayer, J. Boissevain, H. C. Britt, J. R. Nix, A. J. Sierk, P. Grangé, S. Hassani, H. A. Weidenmüller, J. R. Beene, B. Cheynis, D. Drain, R. L. Ferguson, F. E. Obenshain, F. Plasil, G. R. Young, G. A. Petitt, and C. Butler, Phys. Lett. B **176**, 312 (1986).

[3] W. P. Zank, D. Hilscher, G. Ingold, U. Jahnke, M. Lehmann, and H. Rossner, Phys. Rev. C **33**, 519 (1986).

[4] A. Gavron, A. Gayer, J. Boissevain, H. C. Britt, T. C. Awes, J. R. Beene, B. Cheynis, D. Drain, R. L. Ferguson, F. E. Obenshain, F. Plasil, G. R. Young, G. A. Petitt, and C. Butler, Phys. Rev. C **35**, 579 (1987).

[5] D. J. Hinde, R. J. Charity, G. S. Foote, J. R. Leigh, J. O. Newton, S. Ogaza, and A. Chatterjee, Nucl. Phys. **A452**, 550 (1986).

[6] D. J. Hinde, H. Ogata, M. Tanaka, T. Shimoda, N. Takahashi, A. Shinohara, S. Wakamatsu, K. Katori, and H. Okamura, Phys. Rev. C **39**, 2268 (1989).

[7] D. Hilscher, H. Rossner, B. Cramer, B. Gebauer, U. Jahnke, M. Lehmann, E. Schwinn, M. Wilpert, Th. Wilspert, H. Frobeen, E. Mordhorst, and W. Scobel, Phys. Rev. Lett. **62**, 1099 (1989).

[8] J. O. Newton, D. J. Hinde, R. J. Charity, J. R. Leigh, J. J. M. Bokhorst, A. Chatterjee, G. S. Foote, and S. Ogaza, Nucl. Phys. **A483**, 126 (1988).

[9] M. Strecker, R. Wien, P. Plischke, and W. Scobel, Phys. Rev. C **41**, 2172 (1990).

[10] E.-M. Eckert, A. Kühmichel, J. Pochodzalla, K. D. Hildenbrand, U. Lynen, W. F. J. Müller, H. J. Rabe, H. Sann, H. Stelzer, W. Trautmann, R. Trockel, R. Wada, C. Cerruti, P. Lhénoret, R. Lucas, C. Mazur, C. Ngô, M. Ribrag, E. Tomasi, A. Demeyer, and D. Guinet, Phys. Rev. Lett. **64**, 2483 (1990).

[11] E. Mordhorst, M. Strecker, H. Frobeen, M. Gasthuber, W. Scobel, B. Gebauer, D. Hilscher, M. Lehmann, H. Rossner, and Th. Wilpert, Phys. Rev. C **43**, 716 (1991).

[12] M. F. Rivet, D. Logan, J. M. Alexander, D. Guerreau, E. Duek, M. S. Zisman, and M. Kaplan, Phys. Rev. C **25**, 2430 (1982).

[13] L. C. Vaz, D. Logan, E. Duek, J. M. Alexander, M. F. Rivet, M. S. Zisman, M. Kaplan, and J. W. Ball, Z. Phys. A **315**, 169 (1984).

[14] L. Schad, H. Ho, G.-Y. Fan, B. Lindl, A. Pfoh, R. Wolski, and J. P. Wurm, Z. Phys. A **318**, 179 (1984).

[15] J. P. Lestone, J. R. Leigh, J. O. Newton, D. J. Hinde, J. X. Wei, J. X. Chen, S. Elfstrom, and D. G. Popescu, Phys. Rev. Lett. **67**, 1078 (1991).

[16] M. Thonnessen, D. R. Chakrabarty, M. G. Herman, R. Butsch, and P. Paul, Phys. Rev. Lett. **59**, 2860 (1987).

[17] R. Butsch, M. Thoennesen, D. R. Chakrabarty, M. G. Herman, and P. Paul, Phys. Rev. C **41**, 1530 (1990).

[18] R. Butsch, D. J. Hofman, C. P. Montoya, P. Paul, and M. Thoennessen, Phys. Rev. C **44**, 1515 (1991).

[19] H. Ikezoe, N. Shikazono, Y. Nagame, Y. Sugiyama, Y. Tomita, K. Ideno, A. Iwamoto, and T. Ohtsuki, Phys. Rev. C **42**, 342 (1990).

[20] H. Ikezoe, N. Shikazono, Y. Nagame, Y. Sugiyama, Y. Tomita, K. Ideno, A. Iwamoto, and T. Ohtsuki, Phys. Rev. C **42**, R1187 (1990).

[21] V. E. Viola, K. Kwiatkowski, and M. Walker, Phys. Rev. C **31**, 1550 (1985).

[22] D. J. Hinde, J. R. Leigh, J. O. Newton, W. Galster, and S. Sie, Nucl. Phys. **A385**, 109 (1982).

[23] R. J. Charity, J. R. Leigh, J. J. M. Bokhorst, A. Chatterjee, G. S. Foote, D. J. Hinde, J. O. Newton, S. Ogaza, and D. Ward, Nucl. Phys. **A457**, 441 (1986).

[24] A. Gavron, revised version of the code PACE; see Phys. Rev. C **21**, 230 (1980).

[25] F. G. Perey, Phys. Rev. **131**, 745 (1963).

[26] J. R. Huizenga and G. Igo, Nucl. Phys. **29**, 462 (1962).

[27] H. Ikezoe, N. Shikazono, Y. Tomita, Y. Sugiyama, K. Ideno, W. Yokota, Y. Nagame, S. M. Lee, M. Ogihara, S. C. Jeong, H. Fujiwara, and D. J. Hinde, Z. Phys. A **330**, 289 (1988).

[28] R. Vandenbosch and J. R. Huizenga, *Nuclear Fission* (Academic, New York, 1973).

[29] R. P. Schmitt and B. K. Srivastava, Z. Phys. A **335**, 49 (1990).

[30] T. Ericson and V. Strutinski, Nucl. Phys. **8**, 284 (1954).

[31] G. L. Catchen, M. Kaplan, J. M. Alexander, and M. F. Rivet, Phys. Rev. C **21**, 940 (1980).
[32] M. A. McMahan and J. M. Alexander, Phys. Rev. C **21**, 1261 (1980).
[33] M. G. Mustafa, P. A. Baisden, and H. Chandra, Phys. Rev. C **25**, 2524 (1982); A. J. Sierk, Los Alamos National Laboratory Report No. LANL T9.
[34] N. N. Ajitanand, G. La Rana, R. Lacey, D. J. Moses, L. C. Vaz, G. F. Peaslee, D. M. de Castro Rizzo, M. Kaplan, and J. M. Alexander, Phys. Rev. C **34**, 877 (1986).
[35] A. Iwamoto and R. Herrmann, Z. Phys. A **338**, 303 (1991).
[36] D. Ward, R. J. Charity, D. J. Hinde, J. R. Leigh, and J. O. Newton, Nucl. Phys. **A403**, 189 (1983).
[37] W. E. Parker, M. Kaplan, D. J. Moses, G. La Rana, D. Logan, R. Lacey, J. M. Alexander, D. M. de Castro Rizzo, P. DeYoung, R. J. Welberry, and J. T. Boger, Phys. Rev. C **44**, 774 (1991).
[38] B. Fornal, F. Gramegna, G. Prete, G. Nebbia, R. Smith, G. D'Erasmo, L. Fiore, A. Pantaleo, G. Viesti, P. Blasi, F. Lucarelli, I. Iori, and A. Moroni, Phys. Rev. C **41**, 127 (1990).
[39] R. P. Schmitt, G. Mouchaty, D. R. Haenni, and P. Bogucki, Phys. Lett. **127B**, 327 (1983).
[40] F. A. Dilmanian, L. Grodzins, J. W. Ball, M. Beckerman, R. Boisseau, S. Gazes, R. Ledoux, and A. Sperduto, Phys. Lett. **127B**, 172 (1983).
[41] G. La Rana, D. J. Moses, W. E. Parker, M. Kaplan, D. Logan, R. Lacey, J. M. Alexander, and R. J. Welberry, Phys. Rev. C **35**, 373 (1987), and references therein.
[42] R. Lacey, N. N. Ajitanand, J. M. Alexander, D. M. de Castro Rizzo, P. DeYoung, M. Kaplan, L. Kowalski, G. La Rana, D. Loga, D. J. Moses, W. E. Parker, G. F. Peaslee, and L. C. Vaz, Phys. Lett. B **191**, 253 (1987).